Research Article | Vol. 25, No. 15 | 24 Jul 2017 | OPTICS EXPRESS 18092
Optics EXPRESS

Multispectral electroluminescence enhancement of single-walled carbon nanotubes coupled to periodic nanodisk arrays

YURIY ZAKHARKO,[1] MARTIN HELD,[1] ARKO GRAF,[1] TOBIAS RÖDLMEIER,[2] RALPH ECKSTEIN,[2] GERARDO HERNANDEZ-SOSA,[2] BERND HÄHNLEIN,[3] JÖRG PEZOLDT,[3] AND JANA ZAUMSEIL[1,*]

[1]*Institute for Physical Chemistry, Universität Heidelberg, D-69120 Heidelberg, Germany*
[2]*Light Technology Institute, Karlsruhe Institute of Technology, D-76131 Karlsruhe, Germany, InnovationLab, D-69115 Heidelberg, Germany*
[3]*Institut für Mikro- und Nanotechnologie, Technische Universität Ilmenau, D-98693 Ilmenau, Germany*
[*]*zaumseil@uni-heidelberg.de*

Abstract: The integration of periodic nanodisk arrays into the channel of a light-emitting field-effect transistor leads to enhanced and directional electroluminescence from thin films of purified semiconducting single-walled carbon nanotubes. The maximum enhancement wavelength is tunable across the near-infrared and is directly linked to the periodicity of the arrays. Numerical calculations confirm the role of increased local electric fields in the observed emission modification. Large current densities are easily achieved due to the high charge carrier mobilities of carbon nanotubes and will facilitate new electrically driven plasmonic devices.

OCIS codes: (250.5403) Plasmonics; (250.0250) Optoelectronics; (160.4236) Nanomaterials; (250.5230) Photoluminescence.

References and links

1. P. Avouris, Z. Chen, and V. Perebeinos, "Carbon-based electronics," Nat. Nanotechnol. **2**(10), 605–615 (2007).
2. R. B. Weisman and S. M. Bachilo, "Dependence of Optical Transition Energies on Structure for Single-Walled Carbon Nanotubes in Aqueous Suspension: An Empirical Kataura Plot," Nano Lett. **3**(9), 1235–1238 (2003).
3. S. Liang, Z. Ma, N. Wei, H. Liu, S. Wang, and L.-M. Peng, "Solid state carbon nanotube device for controllable trion electroluminescence emission," Nanoscale **8**(12), 6761–6769 (2016).
4. F. Jakubka, S. B. Grimm, Y. Zakharko, F. Gannott, and J. Zaumseil, "Trion Electroluminescence from Semiconducting Carbon Nanotubes," ACS Nano **8**(8), 8477–8486 (2014).
5. J. R. Sanchez-Valencia, T. Dienel, O. Gröning, I. Shorubalko, A. Mueller, M. Jansen, K. Amsharov, P. Ruffieux, and R. Fasel, "Controlled synthesis of single-chirality carbon nanotubes," Nature **512**(7512), 61–64 (2014).
6. H. Liu, D. Nishide, T. Tanaka, and H. Kataura, "Large-scale single-chirality separation of single-wall carbon nanotubes by simple gel chromatography," Nat. Commun. **2**, 309 (2011).
7. M. C. Hersam, "Progress towards monodisperse single-walled carbon nanotubes," Nat. Nanotechnol. **3**(7), 387–394 (2008).
8. Y. Miyauchi, M. Iwamura, S. Mouri, T. Kawazoe, M. Ohtsu, and K. Matsuda, "Brightening of excitons in carbon nanotubes on dimensionality modification," Nat. Photonics **7**(9), 715–719 (2013).
9. X. Ma, N. F. Hartmann, J. K. S. Baldwin, S. K. Doorn, and H. Htoon, "Room-temperature single-photon generation from solitary dopants of carbon nanotubes," Nat. Nanotechnol. **10**(8), 671–675 (2015).
10. F. Pyatkov, V. Fütterling, S. Khasminskaya, B. S. Flavel, F. Hennrich, M. M. Kappes, R. Krupke, and W. H. P. Pernice, "Cavity-enhanced light emission from electrically driven carbon nanotubes," Nat. Photonics **10**(6), 420–427 (2016).
11. R. Miura, S. Imamura, R. Ohta, A. Ishii, X. Liu, T. Shimada, S. Iwamoto, Y. Arakawa, and Y. K. Kato, "Ultralow mode-volume photonic crystal nanobeam cavities for high-efficiency coupling to individual carbon nanotube emitters," Nat. Commun. **5**, 5580 (2014).
12. A. Jeantet, Y. Chassagneux, C. Raynaud, P. Roussignol, J. S. Lauret, B. Besga, J. Estève, J. Reichel, and C. Voisin, "Widely Tunable Single-Photon Source from a Carbon Nanotube in the Purcell Regime," Phys. Rev. Lett. **116**(24), 247402 (2016).
13. X. Ma, O. Roslyak, F. Wang, J. G. Duque, A. Piryatinski, S. K. Doorn, and H. Htoon, "Influence of Exciton

#293067 https://doi.org/10.1364/OE.25.018092
Journal © 2017 Received 18 Apr 2017; revised 21 Jun 2017; accepted 21 Jun 2017; published 19 Jul 2017

Optics EXPRESS

Dimensionality on Spectral Diffusion of Single-Walled Carbon Nanotubes," ACS Nano **8**(10), 10613–10620 (2014).
14. Y. Zakharko, A. Graf, S. P. Schießl, B. Hähnlein, J. Pezoldt, M. C. Gather, and J. Zaumseil, "Broadband Tunable, Polarization-Selective and Directional Emission of (6,5) Carbon Nanotubes Coupled to Plasmonic Crystals," Nano Lett. **16**(5), 3278–3284 (2016).
15. H. M. Doeleman, E. Verhagen, and A. F. Koenderink, "Antenna–Cavity Hybrids: Matching Polar Opposites for Purcell Enhancements at Any Linewidth," ACS Photonics **3**(10), 1943–1951 (2016).
16. X. Yang, A. Ishikawa, X. Yin, and X. Zhang, "Hybrid Photonic-Plasmonic Crystal Nanocavities," ACS Nano **5**(4), 2831–2838 (2011).
17. S. Zou, N. Janel, and G. C. Schatz, "Silver nanoparticle array structures that produce remarkably narrow plasmon lineshapes," J. Chem. Phys. **120**(23), 10871–10875 (2004).
18. L. Shi, T. K. Hakala, H. T. Rekola, J.-P. Martikainen, R. J. Moerland, and P. Törmä, "Spatial Coherence Properties of Organic Molecules Coupled to Plasmonic Surface Lattice Resonances in the Weak and Strong Coupling Regimes," Phys. Rev. Lett. **112**(15), 153002 (2014).
19. J. Y. Suh, C. H. Kim, W. Zhou, M. D. Huntington, D. T. Co, M. R. Wasielewski, and T. W. Odom, "Plasmonic Bowtie Nanolaser Arrays," Nano Lett. **12**(11), 5769–5774 (2012).
20. H. Schokker and A. F. Koenderink, "Statistics of Randomized Plasmonic Lattice Lasers," ACS Photonics **2**(9), 1289–1297 (2015).
21. Y. Zakharko, A. Graf, and J. Zaumseil, "Plasmonic Crystals for Strong Light-Matter Coupling in Carbon Nanotubes," Nano Lett. **16**(10), 6504–6510 (2016).
22. A. Yang, T. B. Hoang, M. Dridi, C. Deeb, M. H. Mikkelsen, G. C. Schatz, and T. W. Odom, "Real-time tunable lasing from plasmonic nanocavity arrays," Nat. Commun. **6**, 6939 (2015).
23. Y. Zakharko, M. Held, A. Graf, T. Rödlmeier, R. Eckstein, G. Hernandez-Sosa, B. Hähnlein, J. Pezoldt, and J. Zaumseil, "Surface Lattice Resonances for Enhanced and Directional Electroluminescence at High Current Densities," ACS Photonics **3**(12), 2225–2230 (2016).
24. T.-Y. Chang, M. Huang, A. A. Yanik, H.-Y. Tsai, P. Shi, S. Aksu, M. F. Yanik, and H. Altug, "Large-scale plasmonic microarrays for label-free high-throughput screening," Lab Chip **11**(21), 3596–3602 (2011).
25. A. E. Cetin, D. Etezadi, B. C. Galarreta, M. P. Busson, Y. Eksioglu, and H. Altug, "Plasmonic Nanohole Arrays on a Robust Hybrid Substrate for Highly Sensitive Label-Free Biosensing," ACS Photonics **2**(8), 1167–1174 (2015).
26. A. J. Baca, J. M. Montgomery, L. R. Cambrea, M. Moran, L. Johnson, J. Yacoub, and T. T. Truong, "Optimization of nanopost plasmonic crystals for surface enhanced Raman scattering," J. Phys. Chem. C **115**(15), 7171–7178 (2011).
27. J. J. Baumberg, T. A. Kelf, Y. Sugawara, S. Cintra, M. E. Abdelsalam, P. N. Bartlett, and A. E. Russell, "Angle-resolved surface-enhanced Raman scattering on metallic nanostructured plasmonic crystals," Nano Lett. **5**(11), 2262–2267 (2005).
28. G. Lozano, D. J. Louwers, S. R. Rodríguez, S. Murai, O. T. Jansen, M. A. Verschuuren, and J. Gómez Rivas, "Plasmonics for solid-state lighting: enhanced excitation and directional emission of highly efficient light sources," Light Sci. Appl. **2**(5), e66 (2013).
29. S. Choi, J. Deslippe, R. B. Capaz, and S. G. Louie, "An Explicit Formula for Optical Oscillator Strength of Excitons in Semiconducting Single-Walled Carbon Nanotubes: Family Behavior," Nano Lett. **13**(1), 54–58 (2013).
30. A. Graf, Y. Zakharko, S. P. Schießl, C. Backes, M. Pfohl, B. S. Flavel, and J. Zaumseil, "Large scale, selective dispersion of long single-walled carbon nanotubes with high photoluminescence quantum yield by shear force mixing," Carbon **105**, 593–599 (2016).
31. S. R.-K. Rodriguez, M. C. Schaafsma, A. Berrier, and J. Gómez Rivas, "Collective resonances in plasmonic crystals: Size matters," Phys. B Condens. Matter **407**, 4081–4085 (2012).
32. A. Christ, T. Zentgraf, J. Kuhl, S. G. Tikhodeev, N. A. Gippius, and H. Giessen, "Optical properties of planar metallic photonic crystal structures: Experiment and theory," Phys. Rev. B **70**(12), 125113 (2004).
33. M. S. Kang and C. D. Frisbie, "A pedagogical perspective on ambipolar FETs," ChemPhysChem **14**(8), 1547–1552 (2013).
34. M. C. Gwinner, S. Khodabakhsh, M. H. Song, H. Schweizer, H. Giessen, and H. Sirringhaus, "Integration of a Rib Waveguide Distributed Feedback Structure into a Light-Emitting Polymer Field-Effect Transistor," Adv. Funct. Mater. **19**(9), 1360–1370 (2009).
35. Y. Zakharko, M. Held, F.-Z. Sadafi, F. Gannott, A. Mahdavi, U. Peschel, R. N. K. Taylor, and J. Zaumseil, "On-Demand Coupling of Electrically Generated Excitons with Surface Plasmons via Voltage-Controlled Emission Zone Position," ACS Photonics **3**(1), 1–7 (2016).
36. M. Rother, S. P. Schießl, Y. Zakharko, F. Gannott, and J. Zaumseil, "Understanding Charge Transport in Mixed Networks of Semiconducting Carbon Nanotubes," ACS Appl. Mater. Interfaces **8**(8), 5571–5579 (2016).
37. B. Auguié and W. L. Barnes, "Collective Resonances in Gold Nanoparticle Arrays," Phys. Rev. Lett. **101**(14), 143902 (2008).
38. M. Hentschel, M. Saliba, R. Vogelgesang, H. Giessen, A. P. Alivisatos, and N. Liu, "Transition from Isolated to Collective Modes in Plasmonic Oligomers," Nano Lett. **10**(7), 2721–2726 (2010).
39. S. R.-K. Rodriguez, O. T. A. Janssen, G. Lozano, A. Omari, Z. Hens, and J. G. Rivas, "Near-field resonance at far-field-induced transparency in diffractive arrays of plasmonic nanorods," Opt. Lett. **38**(8), 1238–1240 (2013).

Optics EXPRESS

40. R. C. McPhedran, L. C. Botten, J. McOrist, A. A. Asatryan, C. M. De Sterke, and N. A. Nicorovici, "Density of states functions for photonic crystals," Phys. Rev. E Stat. Nonlin. Soft Matter Phys. **69**(1), 016609 (2004).
41. M. Ramezani, G. Lozano, M. A. Verschuuren, and J. Gómez-Rivas, "Modified emission of extended light emitting layers by selective coupling to collective lattice resonances," Phys. Rev. B **94**(12), 125406 (2016).
42. S. Murai, M. A. Verschuuren, G. Lozano, G. Pirruccio, S. R. Rodriguez, and J. G. Rivas, "Hybrid plasmonic-photonic modes in diffractive arrays of nanoparticles coupled to light-emitting optical waveguides," Opt. Express **21**(4), 4250–4262 (2013).
43. V. Perebeinos and P. Avouris, "Phonon and electronic nonradiative decay mechanisms of excitons in carbon nanotubes," Phys. Rev. Lett. **101**(5), 057401 (2008).
44. P. B. Johnson and R. W. Christy, "Optical Constants of the Noble Metals," Phys. Rev. B **6**(12), 4370–4379 (1972).

1. Introduction

The demand for new optoelectronic and nanophotonic applications requires novel light sources with tailored optical properties. To this end, semiconducting single-walled carbon nanotubes (SWCNTs) offer a unique combination of high charge carrier mobility [1] and diameter dependent, narrow excitonic transitions at room temperature [2] for the generation of light under electrical pumping [3,4]. Despite the potential spectral tunability over large parts of the near-infrared via the SWCNT diameter and chirality it remains challenging to implement and control large-scale and type-selective growth or purification protocols [5–7]. In contrast to that, specific emission wavelengths can be achieved via the chemical introduction of new emissive states [8,9] or coupling of SWCNTs to resonant electromagnetic cavities [10–14]. The latter allow for the increase of the local photonic density of states at a given energy, and thus, more efficient light emission via the Purcell effect. With regard to such extended spectral and coupling tunability, hybrid photonic-plasmonic cavities are of particular interest as they provide a trade-off between the high quality factors of photonic cavities and the sub-diffraction mode confinement and high local field intensities of plasmonic nanocavities [15,16].

One example is surface lattice resonances (SLRs) that are formed upon far-field coupling between diffraction orders (i.e., photonic modes) and periodically arranged structures that support localized surface plasmon resonances (LSPRs) such as spheres [17], rods [18], bow-ties [19] or disks [14,20–23]. The spectral position of the SLRs, their linewidth and photonic-plasmonic composition are easily controlled by the periodicity of the arrays and spectral position of the LSPRs [17]. Owing to their good quality factors and high electric field intensities, these nanocavities have already led to numerous advances, such as improved sensing of biomolecules [24,25], surface-enhanced Raman scattering [26,27], tailored light emission [14,28], lasing [20,22] and strong light-matter interactions [18,21]. Moreover, by coupling carbon nanotubes to the SLRs, we have successfully demonstrated their spectrally tunable, enhanced and directional photoluminescence [14], as well as a formation of part-light part-matter quasiparticles called plasmon-exciton polaritons [21]. However, due to the intrinsic sensitivity of SLRs to the dielectric environment and charge injecting metal electrodes in particular, the corresponding functionality and integration into electrically driven devices have been limited. Only recently we have established that it is possible to minimize the impact of metallic contacts in electroluminescent devices by utilizing the planar arrangement of source-drain electrodes in polymer light-emitting field-effect transistors (LEFETs) such that far-field coupling was not affected [23]. A similar approach using SWCNTs as a material for high-mobility charge transport and near-infrared light-emission is highly desirable as it would allow us to strongly modify and enhance their electroluminescence and would bring new functionalities and characteristics to electrically driven devices supporting SLRs.

Here, we implement periodic gold nanodisk arrays supporting SLRs into LEFETs with (6,5) SWCNT thin films to tailor their photo- and electroluminescence (EL) characteristics. We were able to enhance the emitted light from three spatially separated regions within a single channel of a LEFET in the 1000-1500 nm spectral range with distinct hybrid photonic-

Optics EXPRESS

plasmonic resonances. As confirmed by angle-resolved spectroscopy, electroluminescence also exhibited a large directionality with divergence angles as small as ~6.5°. Our experimental data together with numerical simulations implicate the increase of the fractional local density of states as the main origin of the observed modification of intensity and angular redistribution of light emission. The large current densities (30 kA·cm^{-2}) in SWCNT LEFETs and the high exciton oscillator strength of SWCNTs [29] may open a path toward electrically pumped carbon-based photon or polariton lasers.

2. Device design and fabrication

To demonstrate control over light emission from SWCNTs under electrical pumping we integrated gold nanodisk arrays into a LEFET as schematically shown in Fig. 1(a). The fabrication of a top-gate, bottom-contact LEFET started with patterning three representative nanodisk arrays (over a 20 × 150 μm^2 area each) via electron-beam lithography onto a glass substrate. For electrical insulation the nanodisks were covered with a 1 nm aluminum oxide layer. The gold source and drain electrodes of the LEFET were patterned photolithographically around the nanodisk arrays. Next, a 14 nm film of polymer-sorted (6,5) SWCNTs [30] was spin-coated on top as the transport and emission layer. The quasi-monochiral SWCNT layer was selected to facilitate interpretation of the spectral changes associated with the SLRs. The device was completed with a hybrid gate dielectric (226 nm of poly(methyl methacrylate), 38 nm hafnium oxide and 5 nm aluminum oxide) and a 200 nm thick PEDOT:PSS gate electrode (sheet resistance 110–150 Ω·sq^{-1}), deposited by aerosol jet printing. The conductivity of the PEDOT:PSS is sufficiently high for the application of a gate potential, but at the same time allows us to keep the change in the refractive index along the different layers to a minimum (see Appendix for more details on sample fabrication). This optimized stack configuration with an effective refractive index close to n = 1.5 (defined by the bottom glass, the top PMMA and PEDOT:PSS layers) does not negatively affect the performance of SLRs, as reported recently [23]. The number of nanodisks in the arrays defined by their area and periodicity was sufficiently large to provide reasonable collective coupling of the nanodisks and thus high quality of the SLRs [31].

In addition to the transistor channel with the nanodisk arrays, we also fabricated a reference channel nearby to directly compare electrical and optical characteristics of the corresponding LEFETs, as visualized by the dark-field image under white light illumination in Fig. 1(b). Scanning electron micrographs show the square lattice arrangement of nanodisks with periodicities of a = 700, 850 and 1000 nm and nanodisk diameters of ~230, 265 and 300 nm, respectively. The periodicity and the size of the nanodisks were designed with the aim to form high quality SLRs and to demonstrate their tunability in a representative ~1100-1500 nm spectral range. First, for a homogeneous environment with refractive index n, the Rayleigh anomalies associated with the diffractive coupling of LSPRs occur for normal directions at λ = a × n or ~1050, 1275 and 1500 nm for the arrays under investigation [32]. Second, the size of the nanodisks enables the control of spectral overlap between LSPRs and Rayleigh anomalies, and thus the magnitude, the damping properties and the quality factors of the formed SLRs [17].

Upon application of voltage to the gate and drain electrodes (the source electrode is grounded) of the LEFET [Fig. 1(a)] charge carriers start to accumulate in the SWCNTs layer. Depending on the relative magnitude and sign of the applied gate potential with respect to the source and drain electrodes, electrons and holes can be injected into the SWCNTs from either electrode, which is a property of ambipolar semiconductors and transistors in general [33]. The injection of both carriers from opposite electrodes defines a narrow zone within the channel where electrons and holes meet and form excitons that eventually recombine and emit light. An important feature of such an ambipolar LEFET is that the number of formed excitons, which controls the intensity of the emitted light, is determined by the drain-source current because all holes and electrons have to recombine, when the emission zone is located

Optics EXPRESS

away from the electrodes. The planar structure of LEFETs has also proven to be very robust against the integration of dielectric waveguides [34] and plasmonics structures [35]. A comparison of the drain current versus gate voltage, i.e., transfer characteristics, for transistor channels with and without nanodisks is shown in Fig. 1(c). Although an increase of the drain current is evident for the channel with nanodisks, the overall performance of the devices remained almost unchanged (see Appendix, Fig. 4, Table 1 and Fig. 5) for threshold voltages, hole and electron mobilities, output curves and transfer characteristics at low source-drain bias). The external emission efficiency of the fabricated LEFETs was comparable to reference devices of known external quantum efficiency of ~10^{-5} photons per injected charge carrier and thus similar to state of the art values for electrically driven emission from carbon nanotubes (10^{-4} – 10^{-6} photons/electron) [3,4,10].

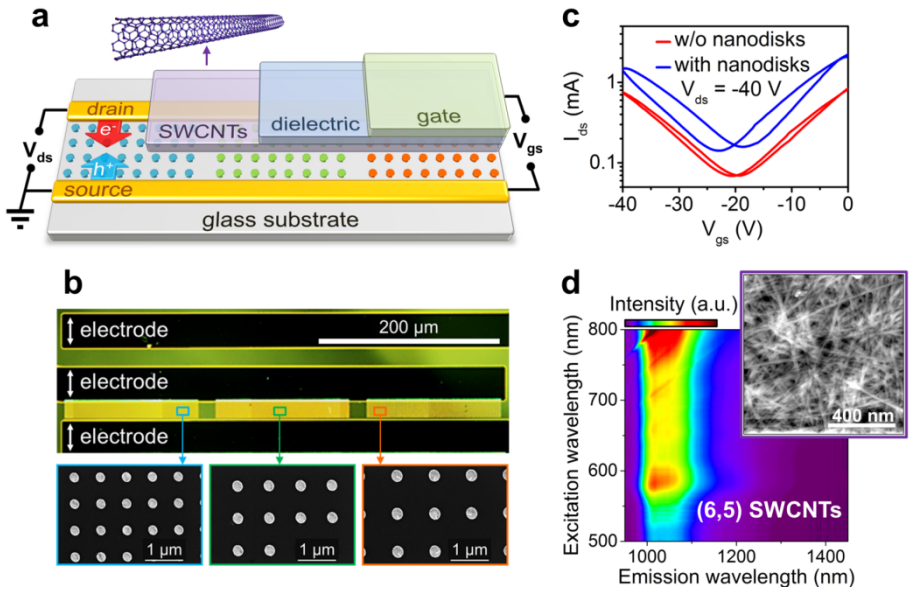

Fig. 1. (a) Schematic geometry and operation principle of a top-gated light-emitting field-effect transistor (LEFET). (b, top) Dark-field optical micrograph of a LEFET under white-light illumination showing edges of source and drain electrodes and the channel filled with periodic arrays of gold nanodisks with 700, 850 and 1000 nm pitch (diameter 230, 265 and 300 nm, respectively) and their corresponding scanning electron micrographs. (c) Ambipolar transfer characteristics of LEFETs without (red) and with (blue) gold nanodisks arrays in the channel. (d) Photoluminescence excitation-emission map of the SWCNT layer within the LEFET (inset: representative atomic-force micrograph of the SWCNT layer).

Before looking at light emission from the SWCNTs coupled to the nanodisks under electrical excitation, we investigated the photoluminescence (PL) response of a thin layer of SWCNTs within the channel without any nanodisks. As shown in Fig. 1(d) the pronounced spectral feature in the PL excitation-emission map can be easily associated with the (6,5) SWCNTs and their corresponding E_{22} excitonic transition (absorption at 577 nm). As for emission, the corresponding E_{11} transition is slightly redshifted and broadened (~1050 nm, full-width at half maximum ~130 nm) compared to the typical values of ~1020 nm and 40 nm, respectively, for thin films of (6,5) SWCNTs [14]. This apparent shift and broadening are most likely related to partial energy transfer from the majority of (6,5) SWCNTs to a few SWCNTs with larger diameters such as (7,5) nanotubes that were abundant in the raw CoMoCAT material (visible as the shoulder at ~1050 nm) [36]. Although they cannot be distinguished as specific E_{22} transitions in the PL excitation-emission map fast energy transfer and emission from these SWCNTs are facilitated by the very low polymer content for dense SWCNT films. The typical PL efficiency for these films is ~0.1% with exciton lifetimes of a

Optics EXPRESS

few picoseconds, as reported recently [14]. The length of the SWCNTs is about 1 μm as evaluated from the atomic-force micrograph [see inset in Fig. 1(d)].

3. Results

To demonstrate the tunability and angular dispersion characteristics of light emission from SWCNTs coupled to the nanodisk arrays with different pitch, we performed angle-dependent measurements: for PL with laser excitation at λ = 640 nm (power ~10 mW) and EL at a current density of J_{ds} ~10-30 kA·cm^{-2} (taking into account a channel width of 500 μm and an estimated accumulation layer thickness of 2 nm). To enable acquisition of wavelength and angular distribution of the collected light in a single measurement we used an objective back-focal plane imaging technique as reported recently (see Appendix for details) [14]. With this approach the entrance slit of the spectrometer defines the collection plane, detection angle θ and the polarization state of the light. In general, due to the square symmetry of the fabricated arrays and thus equal pitch for the two orthogonal directions, the optical response for the entrance slit oriented along either direction of the arrays should be the same. However, the long axis of the rectangular arrays [i.e., 150 μm versus 20 μm for the short side, see Fig. 1(b)] hosts a larger number of nanodisks, and thus the SLRs formed via coupling along this direction show higher quality factors.

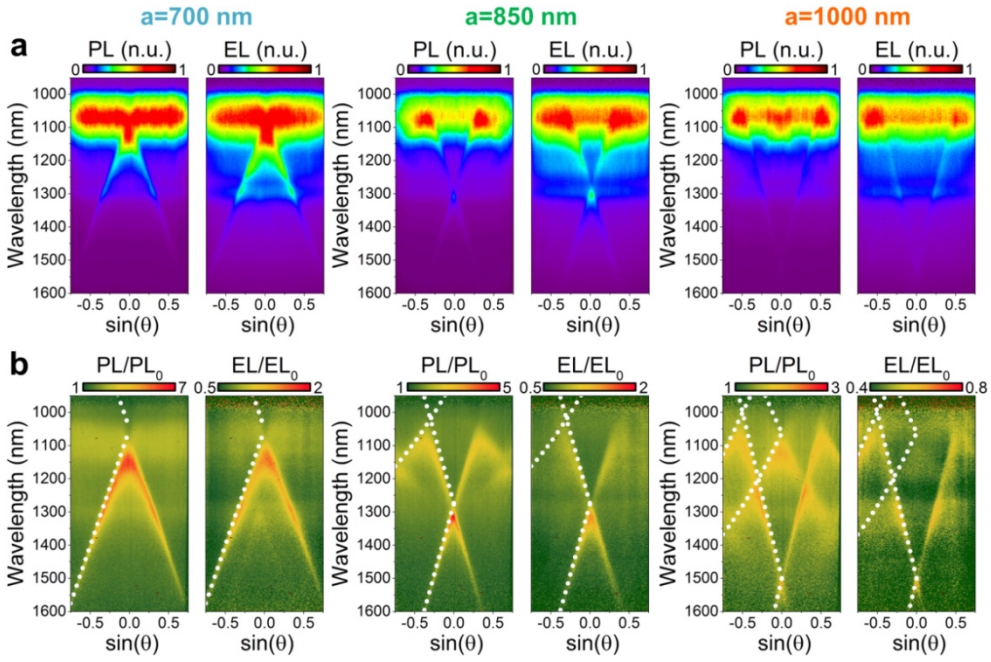

Fig. 2. Angle-resolved TE-polarized photo- and electroluminescence spectra (a) and enhancement factors (b) for regions with nanodisk arrays with pitch 700, 850 and 1000 nm (from left to right). Analytical dependencies for Rayleigh anomalies at negative angles are indicated with white dotted lines.

The collected angle-dependent PL and EL spectra for the transverse-electric (TE) polarizations and three nanodisk arrays with pitches 700, 850 and 1000 nm (from left to right) are shown in Fig. 2(a). The corresponding data for the transverse-magnetic (TM) polarization can be found in the Appendix (Fig. 6). One can clearly see that the optical response under photo- and electrical excitation is dominated by the dispersionless emission of the SWCNTs with excitonic transitions at ~1070 nm that are also visible for the transistor channel without nanodisk arrays (see Appendix Fig. 7). More importantly, there are additional highly dispersive spectral features characterized by the crossing point at zero angle that change their

Optics EXPRESS

spectral positions for different pitches. To facilitate interpretation of these features, we calculated the experimental PL and EL enhancement factors defined as the ratio of light emission with and without nanodisks as shown in Fig. 2(b). Here, all EL values were normalized by current density; J_{ds} ~30 kA·cm^{-2} for the channel with nanodisks and J_{ds} ~10 kA·cm^{-2} for the reference. This correction gives a proper evaluation of the enhancement factors assuming constant internal quantum efficiency of excitons within the given range of current densities. In order to correlate the new features with the anticipated position of the SLRs, the analytical curves of (+ 1,0) and (−1,0) Rayleigh anomalies are indicated by white dotted lines, taking into account the refractive index of the environment (n = 1.5) and the nanodisk array pitch [21]. The observed resonances are slightly redshifted, which is common due to Fano-like interactions between broad LSPRs and narrow Rayleigh anomalies [17,37]. Moreover, at short wavelengths, the higher order (± 1, ± 1) and (± 2,0) Rayleigh anomalies are also visible for the 850 and 1000 nm arrays. The divergence of the TE-polarized emission for normal direction was estimated as the full-width at half maximum of the enhancement factor for the representative 850 nm pitch array [i.e., cross section in Fig. 2(b) at 1320 nm] and is within ~6.5°. For the TM-polarized emission the new spectral features are associated with (0, ± 1) Rayleigh anomalies as shown in the Appendix (Fig. 6). The typical full-width at half maximum (FWHM) of the peaks over the detection range reaches values as small as 20 nm for TE-polarized light indicating high quality resonances (Q = λ/FWHM ~1300/20 = 65). For TM-polarized light, the quality factors tend to be slightly smaller (Q ~1300/40 = 32.5), due to fewer nanodisks coupling for these Rayleigh anomalies, that is, perpendicular to the detection plane and along the shorter axis of the nanodisk array. This variation of quality factors for two orthogonal directions is further confirmed when the sample is rotated by 90° (see Appendix Fig. 8). In this case, the TE-polarized light exhibits smaller quality factors, as it now reflects coupling for the shorter axis of the arrays. Nevertheless, one can clearly see that SLRs can be efficiently used to modify light emission with nanodisk arrays as small as 20 μm.

4. Discussion

Regarding the absolute values of the observed enhancement, we note that emission enhancement under electrical excitation is systematically lower (even below 1 for some regions) than for the optically excited SWCNTs. In terms of the expected Purcell effect being responsible for the enhanced emission, the excitation mechanism (EL or PL) should not be important. The main reason for this discrepancy is the current density normalization for the EL data, as the used current values account for the whole LEFET channel and may not reflect the local current density between nanodisks in each array, which would be necessary for more precise correction factors. To visualize the emission control and to exclude the variation of the current densities through nanodisk arrays, we normalize (at 1070 nm) and compare the EL signal detected normal to the substrate (θ = 0°) of pure SWCNTs with signal from the regions with nanodisks (see Appendix, Fig. 9, top panel). Although the absolute intensities of the new spectral features are smaller than from the bare SWCNTs they can be clearly distinguished. The narrow lineshape and tunability of the spectral position are further verified by subtraction of the reference spectrum and normalization as shown in Appendix Fig. 9 (bottom).

To elaborate more on the exact mechanism of the observed enhancement, the PL enhancement factors for two detection angles, i.e., at θ = 0° and 10° for the nanodisk array with pitch 850 nm are plotted in Fig. 3(a) (top panel). In addition, we include the comparison of the reflectivity data for the same region and angles of detection in Fig. 3(a) (bottom). The angle and polarization-resolved reflectivity data, were recorded as reported previously [14], and is defined as the difference between the signals from the channels with and without the nanodisk array and normalized by the spectrum of a 100% reflecting surface illuminated with a lamp (see Appendix Fig. 10 for full set of reflectivity data). It is interesting to note that the maximum of the enhancement does not correlate with the reflectivity peak position (it is

Optics EXPRESS

blueshifted) as one would expect if the emission enhancement were a result of increased scattering and/or outcoupling of light in one particular direction. This mechanism can be excluded further by taking into account the random but in-plane orientation of SWCNTs (length ~1 μm) in a thin layer (~14 nm), and thus the lack of light trapping issues in these LEFETs that may be alleviated by scattering of SLRs. Instead, the observed blue-shifted emission enhancement (compared to maximum reflectivity) corresponds to the trade-off between maximum local field enhancement for the wavelengths corresponding to suppressed radiative damping [38,39] and efficient coupling to the far-field at the maximum reflectivity.

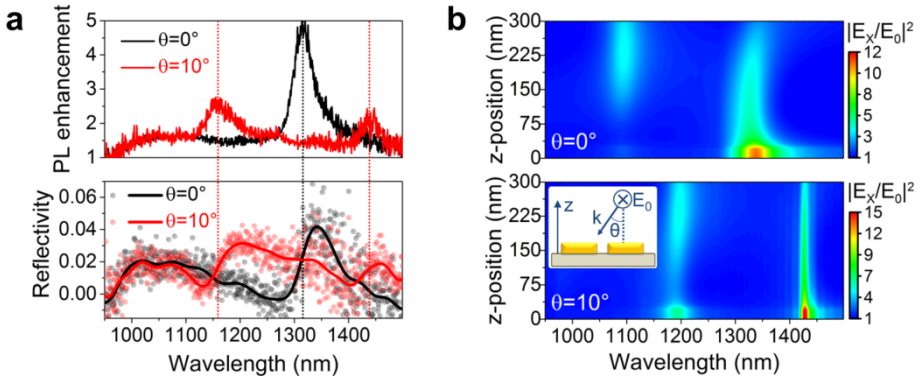

Fig. 3. (a) (top) PL enhancement spectra of the region with 850 nm array pitch at emission angles θ = 0° (black) and θ = 10° (red). (bottom) Corresponding reflectivity spectra with scattered symbols representing experimental values and solid lines are smoothed data for clarity. (b) FDTD calculated area-averaged field intensity enhancement for various plane-substrate separations and angle of incidence θ = 0° (top) and θ = 10° (bottom) according to the simulation schematic in the inset.

It is important to note that local field enhancements for the Purcell effect correspond to an increase of the local density of states (LDOS), increased radiative decay rate of emitters and thus higher emission efficiency. However, for our system with wide angular dispersion characteristics it is more relevant to consider the density of states proportional to the power emitted in one particular direction, referred to as the spectral density of states [40] or fractional radiative local density of states (FLDOS) [41]. Although the increase of FLDOS does not necessarily imply an increase of LDOS, we integrated emission over all collection angles accessible by the objective (± 50°) to quantify any variation of LDOS and the Purcell effect as such [see Appendix, Fig. 11(a)]. In general, this integration should be performed over all emission angles (i.e., whole 4π solid angle), but PL data for channels with and without nanodisks already provide clear evidence that the total emitted power with an nanodisk array is higher than without, and thus the role of the Purcell effect can be corroborated. Ideally, the shortening of the exciton lifetime should be observed as the ultimate experimental verification of the Purcell effect, but due to the already very short lifetimes of SWCNTs (<10 ps) [14] further shortening would be very challenging to measure. More importantly, since the angle-integrated PL enhancement [see Appendix, Fig. 1(b)] shows wavelength dependence with an off-resonance enhancement (at λ ~950 nm and >1500 nm) close to 1 (i.e., no enhancement), we can also exclude any effect of increased laser excitation rate. For the opposite situation, wavelength-independent emission enhancement and/or higher off-resonance values would be expected. Moreover, this mechanism is not relevant for the modified emission under electrical excitation.

In order to gain further insight into the increase of FLDOS, we performed numerical simulations of the field intensity enhancement around the nanodisks. We took advantage of the Lorentz reciprocity theorem connecting the increase of power emitted by the dipole in a particular direction and the enhancement of the local fields upon plane wave illumination

Optics EXPRESS

from this direction [41]. Since the observed PL or EL emission originates from the SWCNTs evenly distributed around the nanodisks and are thus affected by the different magnitudes of the local fields, the enhancement of local fields should also be averaged over different positions. To estimate the versatility of the emission enhancement using nanodisk arrays we performed averaging for planes at different distances from the glass-SWCNTs interface. With this approach the increase of FLDOS for emitters at different distances from the substrate surface, e.g., for a much thicker SWCNTs layers, are directly visualized in Fig. 3(b). Here, the calculated values for each plane are plotted versus the distance (z) from the surface for detection/emission angles of 0° and 10°. First, one can clearly see the correlation between peak positions observed in the experimental [Fig. 3(a), top] and simulated data. Second, although the enhancement tends to decrease for emitters further away from the nanodisks, it is still reasonably high even at distances as large as 300 nm, which is a direct manifestation of the photonic component of the hybrid photonic-plasmonic SLRs. For a separation larger than 100 nm a second peak corresponding to the quasi-guided mode [42] is expected (~1100 nm). However this peak is not observed for our 14 nm thick layer. It is important to note that the experimentally calculated enhancement values are smaller than the values expected from the simulated fields. The most probable origin of this deviation is differences between simulated and fabricated structures, such as the quality/uniformity of the nanodisks, presence of additional interfaces and possibly electric field screening effects caused by the dense SWCNT film. Furthermore, the metal-related losses close to the nanodisks may compete with the radiative decay and thus decrease the experimental emission enhancement. As illustrated by the simulated three-dimensional field distribution around nanodisks, shown in Appendix Fig. 12, the highest field intensities still tend to be in the vicinity of the nanodisks despite generally delocalized mode profiles of the SLRs.

It is worth noting that for clarity and as a proof of concept the demonstrated emission enhancement was designed to affect the rather weak light emission from the carbon nanotubes in the 1100-1500 nm spectral range (likely originating from the multiphonon-assisted relaxation) [43]. Hence, despite the enhancement, the brightness of the new spectral features shifted from the main excitonic transitions remains low. To achieve higher absolute intensities, one may utilize a selection of multichiral but semiconducting SWCNT networks. Alternatively, strong light-matter coupling becomes possible for higher density and/or larger thickness of the SWCNT layer with light emission channeled into plasmon-exciton polariton states [21].

5. Summary

In conclusion, we have shown that nanodisk arrays supporting SLRs enable highly directional and enhanced electroluminescence from SWCNTs in a planar light-emitting field-effect transistor operating at high current densities. The presented experimental and numerical data confirm that the emission enhancement is due to the combination of increased radiative decay of generated excitons via the Purcell effect and the redirection of emission following the angular dispersion properties of the SLRs. Due to the small footprint of these arrays it was possible to integrate three different nanodisk arrays within a single LEFET channel and to generate light with distinct spectral and angular emission characteristics. This is an important step toward efficient, tunable, directional and electrically driven light sources in the near-infrared. With their high charge carrier mobilities and thermal stability supporting very high current densities, as well as narrow excitonic transitions SWCNTs represent an excellent material for a variety of exciting plasmon-assisted interactions, such as electrically pumped lasing or plasmon-exciton polariton condensation.

Optics EXPRESS

Appendix

LEFET fabrication

Gold nanodisks were produced by electron-beam lithography on glass (Schott AF32 Eco) with a Raith 150 system (Raith GmbH) as reported recently [23]. To form a thin aluminum oxide layer on top of the nanodisks, 1 nm of aluminium was evaporated and left to oxidize in air. Photolithography followed by electron-beam evaporation of 2 nm Cr/30 nm Au and lift-off was employed to pattern the source-drain electrodes with a channel length of 20 µm and width of 500 µm around the nanodisk arrays. (6,5) SWCNTs were prepared from CoMoCAT raw material by selective polymer dispersion in toluene as discussed previously [30]. 50 µL of a highly concentrated SWCNT dispersion in toluene was spincoated twice at 1000 rpm for 60 s and annealed at 300 °C in dry nitrogen for 60 min to form a 14 nm dense and randomly oriented SWCNT film as a charge transport and light emitting layer. The hybrid dielectric consisted of three layers: poly(methyl methacrylate) (PMMA), hafnium oxide (HfOx) and aluminium oxide (AlOx). Syndiotactic PMMA (Polymer Source, Mw = 300 kg·mol^{-1}) was dissolved in anhydrous n-butyl acetate (50 mg·mL^{-1}) and stirred at 80 °C for 180 min. The PMMA layer was spincoated at 4000 rpm for 60 s, resulting in a film thickness of 230 nm. A 38 nm HfO_x layer was added by atomic layer deposition (ALD, Ultratech Savannah S100) using tetrakis(dimethylamino)hafnium as a hafnium precursor at 100 °C and water as an oxygen source. HfO_x acted as an encapsulation barrier to stop the diffusion of H_2O from the PEDOT:PSS to the interface of the PMMA and the SWCNTs. To prevent etching of HfO_x by PEDOT:PSS, a thin AlO_x layer was deposited by ALD with trimethylaluminium as an aluminium precursor and water at 80 °C.

The conductive polymer PEDOT:PSS was used for the gate electrode. A pH-neutral high conductivity PEDOT:PSS dispersion (Sigma Aldrich, Orgacon N-1005, 0.83% in H_2O) with a small addition of Triton-X-100 surfactant (Sigma Aldrich) was printed with an Optomec Aerosol Jet Printer (carrier gas flow 25-30 ccm, sheeth gas flow 6-8 ccm, stage temperature 60 °C, nozzle speed 5 mm·s^{-1}, line pitch 20 µm), yielding a film thickness of approximately 200 nm. The pH-neutral PEDOT:PSS did not etch the underlying dielectric layer. To avoid additional degradation, all devices were encapsulated for optoelectronic measurements with a glass cover slip and epoxy resin.

Characterization

Surface morphology of SWCNT film was characterized by atomic-force microscopy in Scan Asyst mode (Bruker Dimension Icon). Current-voltage characteristics were recorded with an Agilent 4156C Semiconductor Parameter Analyzer or a Keithley 2612A source meter. Gate dielectric capacitances were determined with an Agilent E4980A Precision LCR Meter. The photoluminescence-excitation map was obtained by excitation of the SWCNT film with a wavelength tunable (1 nm step with laser-line tunable filter, Fianium Ltd.) output of a supercontinuum laser source (WhiteLase SC400, Fianium Ltd.) and detection with an Acton SpectraPro SP2358 spectrometer (grating 150 lines·mm^{-1}) and a liquid nitrogen cooled InGaAs line camera (PI Acton OMA V:1024 1.7). The obtained signal was wavelength calibrated for sensitivity of the detection system and incident laser power (measured with a calibrated silicon photodiode power sensor). For angle- and wavelength-dependent spectroscopy, we used a Fourier-space imaging setup, as reported previously [14]. Briefly, for reflectance or photoluminescence spectroscopy, a collimated white light source or laser beam (λ=640 nm; continuous wave power 10 mW) was passed through a 50:50 beam-splitter and then focused on the sample down to a 1-2 µm spot size by a ×100 near-infrared objective with 0.8 numerical aperture. The back-focal plane of the objective was imaged via Fourier optics and a tube lens onto the entrance slit of a spectrometer (IsoPlane SCT-320, Princeton Instruments) equipped with a TE-cooled 2D InGaAs camera (640×512 pixels NIRvana 640ST, Princeton Instruments). Scattered laser light was blocked by a long pass filter with an

Optics EXPRESS

850 nm cutoff wavelength. An additional polarizer was placed in front of the spectrometer to select transverse-electric or transverse-magnetic light polarization. The same setup was used to acquire angle-dependent electroluminescence spectra. All spectra were corrected with respect to the response of the detection system with a calibrated tungsten halogen lamp.

3D finite-difference time-domain calculations

For 3D finite-difference time-domain (FDTD) simulations a commercial software (FDTD Solution v8.16.884, Lumerical Solutions Inc., Canada) was used. The simulation region (boundaries defined by periodic conditions and perfectly matched layers) included the glass substrate, gold nanodisk (h=25 nm, D=260 nm) and 500 nm of SWCNTs/PMMA with n=1.5. To reduce computational resources and computational time, we took advantage of the symmetric/antisymmetric boundary conditions where possible. A uniform mesh size of 2.5 nm (X, Y and Z-directions) was used in the region (X×Y×Z=850×850×400 nm^3) around gold nanodisk. Outside of these regions the grid was defined by the auto non-uniform mesh technique. The optical constants of gold were obtained from Johnson and Christy [44].

In order to estimate field intensity enhancement profiles we recorded electromagnetic fields with 2D profile monitors in X–Y, X–Z, and Y–Z planes (Appendix, Fig. 12). Field intensity enhancement $|E_x/E_0|^2$ was calculated for a plane wave injected at θ=0° or 10° to the surface (X-polarized) taking into account the values for the configuration without the gold nanodisk. Analogously, for the plane-averaged field intensity enhancement values as a function of the distance from the glass/SWCNTs interface [Fig. 3(b)] the electromagnetic fields were recorded with a 3D monitor (X×Y×Z=850×850×300 nm^3) set around the gold nanodisk. Further, the enhancement was calculated by averaging values in the X-Y plane for each Z-position excluding values of cells/positions not representing SWCNTs layer and dividing by the values for the structure without the gold nanodisk.

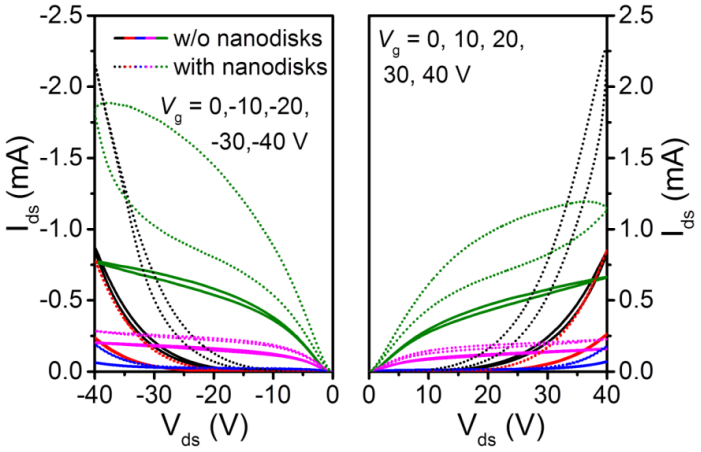

Fig. 4. Comparison of ambipolar output characteristics of LEFETs with (dotted lines) and without (solid lines) nanodisk arrays.

Table 1. Extracted charge transport parameters (linear mobility μ_{lin} and threshold voltages V_{Th} for holes and electrons) for LEFETs with and without nanodisk array in the channel.

	$\mu_{lin,h}$ ($cm^2V^{-1}s^{-1}$)	$V_{Th,h}$ (V)	$\mu_{lin,e}$ ($cm^2V^{-1}s^{-1}$)	$V_{Th,e}$ (V)
without nanodisk array	12.5	−30.0	2.0	14.0
with nanodisk array	3.4	−12.7	4.3	11.8

Optics EXPRESS

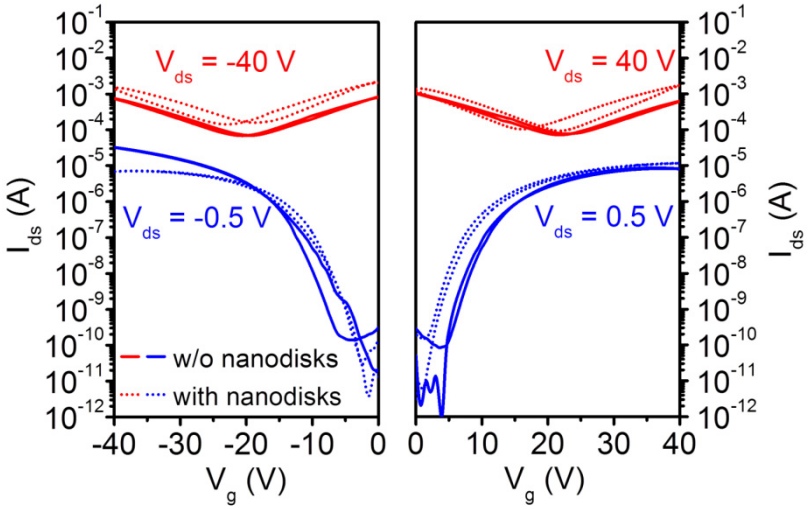

Fig. 5. Ambipolar transfer characteristics of LEFETs with (dotted lines) and without (solid) gold nanodisks arrays at high (red) and low (blue) source-drain voltage. The latter show almost no hysteresis and high (~10^5-10^6) on/off ratios, thus corroborating the absence of any metallic carbon nanotubes.

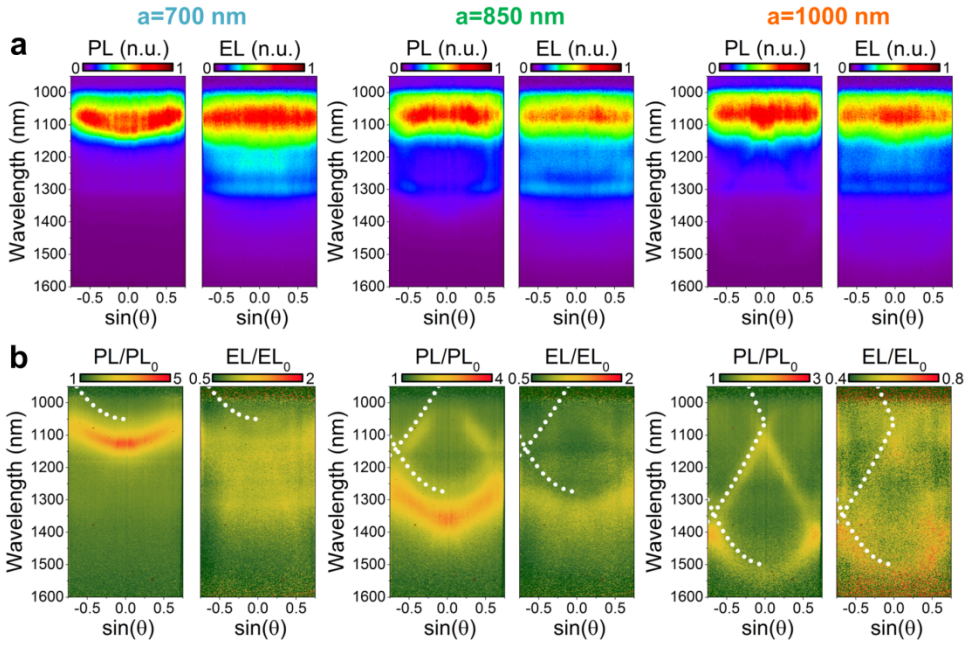

Fig. 6. Angle-resolved TM-polarized photo- and electroluminescence spectra (a) and enhancement factors (b) for regions with nanodisk array pitch 700, 850 and 1000 nm (from left to right). Analytical dependencies for Rayleigh anomalies at negative angles are indicated with white dotted lines.

Optics EXPRESS

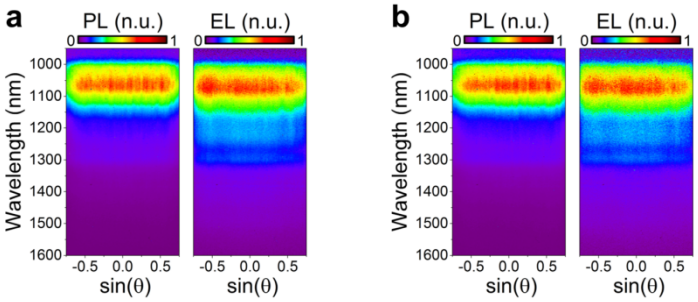

Fig. 7. Angle-resolved TE (a) and TM-polarized (b) photo- and electroluminescence spectra for channel region without nanodisk array.

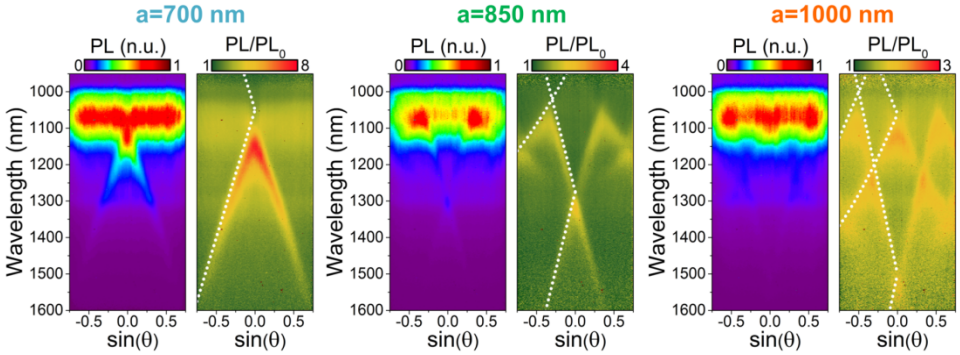

Fig. 8. Angle-resolved TE-polarized photoluminescence spectra and enhancement factors for regions with nanodisk array pitch 700, 850 and 1000 nm (from left to right). Detection plane was rotated by 90° to probe the short side of the arrays. Analytical dependencies for Rayleigh anomalies at negative angles are indicated with white dotted lines.

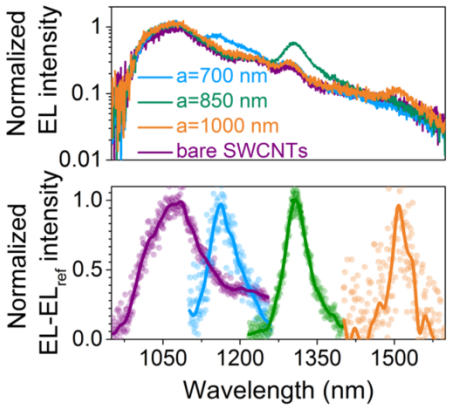

Fig. 9. Normalized to E_{11} transition (top) and normalized differential (bottom) EL spectra of pure SWCNTs (purple) and emission from the regions with array pitch 700 (blue), 850 (green), and 1000 nm (orange) normal to the sample surface.

Optics EXPRESS

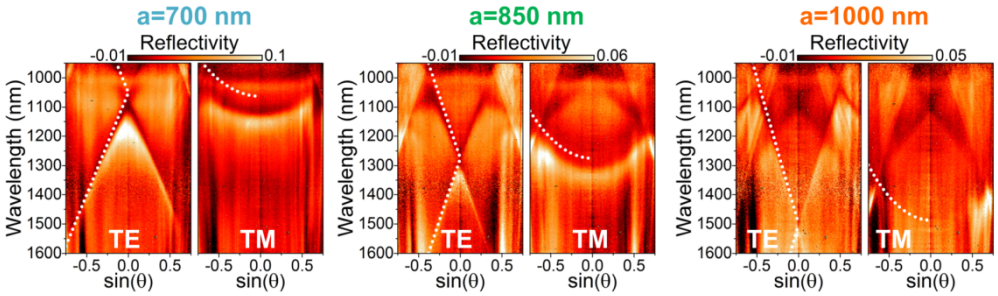

Fig. 10. Angle- and polarization-resolved reflectivity spectra for regions with nanodisk array pitch 700, 850 and 1000 nm (from left to right). Analytical dependencies for Rayleigh anomalies at negative angles are indicated with white dotted lines.

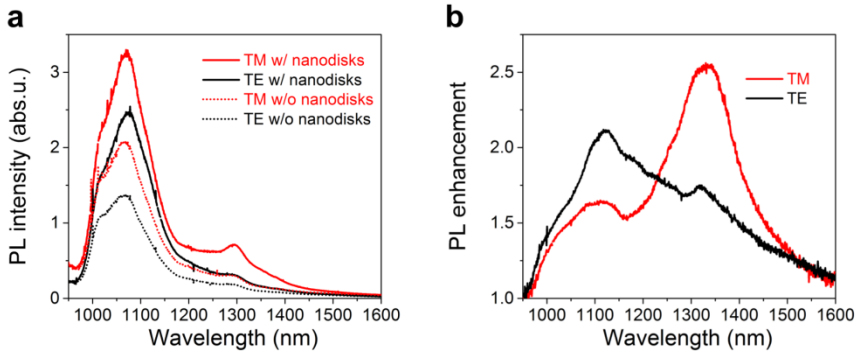

Fig. 11. (a) Angle-integrated TE (black) and TM-polarized (red) photoluminescence intensity of the SWCNTs without (dotted line) and with (solid) 850 nm pitch periodic array of gold nanodisks. (b) Corresponding photoluminescence enhancement values.

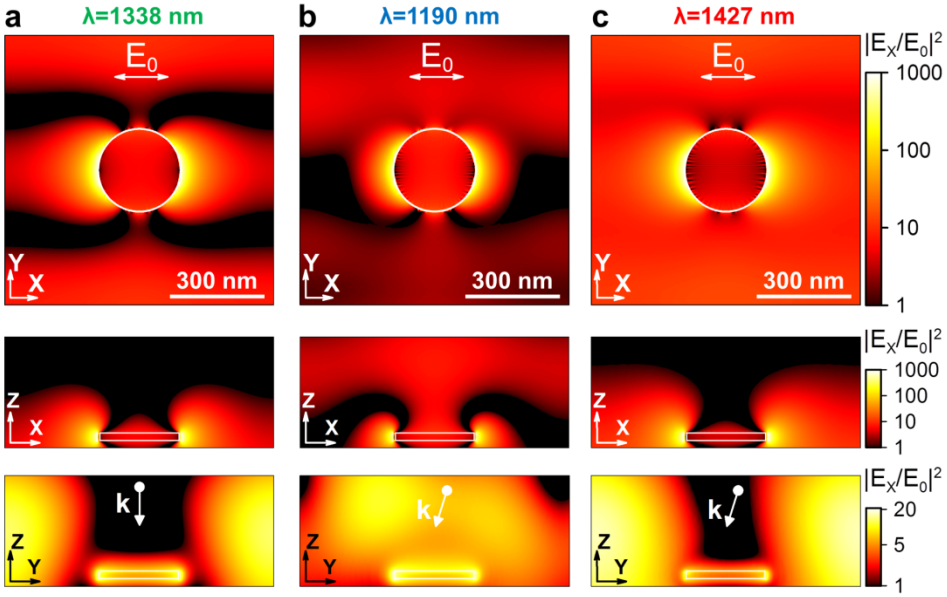

Fig. 12. Calculated electric field intensity enhancement distribution (X–Y, X–Z, and Y–Z planes, from top to bottom, respectively) around a single gold nanodisk in a periodic array with pitch 850 nm at incidence angle of the plane wave θ = 0°, for λ = 1338 nm (a); θ = 10°, for λ = 1190 nm (b) and λ = 1427 nm (c).

Optics EXPRESS

Funding

The European Union's Seventh Framework Programme (FP/2007-2013)/ERC Grant Agreement No. 306298 (EN-LUMINATE). The German Ministry of Education and Research (FKZ: 13N13691).